



**HAL**  
open science

## Increased production of cosmogenic $^{10}\text{Be}$ recorded in oceanic sediment sequences: Information on the age, duration, and amplitude of the geomagnetic dipole moment minimum over the Matuyama–Brunhes transition

Quentin Simon, Nicolas Thouveny, Didier Bourlès, Franck Bassinot, Tatiana Savranskaia, Jean-Pierre Valet

### ► To cite this version:

Quentin Simon, Nicolas Thouveny, Didier Bourlès, Franck Bassinot, Tatiana Savranskaia, et al.. Increased production of cosmogenic  $^{10}\text{Be}$  recorded in oceanic sediment sequences: Information on the age, duration, and amplitude of the geomagnetic dipole moment minimum over the Matuyama–Brunhes transition. *Earth and Planetary Science Letters*, 2018, 489, pp.191-202. 10.1016/j.epsl.2018.02.036 . hal-01735837

**HAL Id: hal-01735837**

**<https://hal.science/hal-01735837v1>**

Submitted on 16 Mar 2018

**HAL** is a multi-disciplinary open access archive for the deposit and dissemination of scientific research documents, whether they are published or not. The documents may come from teaching and research institutions in France or abroad, or from public or private research centers.

L'archive ouverte pluridisciplinaire **HAL**, est destinée au dépôt et à la diffusion de documents scientifiques de niveau recherche, publiés ou non, émanant des établissements d'enseignement et de recherche français ou étrangers, des laboratoires publics ou privés.



Distributed under a Creative Commons Attribution - NonCommercial - NoDerivatives 4.0 International License



# Increased production of cosmogenic $^{10}\text{Be}$ recorded in oceanic sediment sequences: Information on the age, duration, and amplitude of the geomagnetic dipole moment minimum over the Matuyama–Brunhes transition

Quentin Simon<sup>a,b,\*</sup>, Nicolas Thouveny<sup>a</sup>, Didier L. Bourlès<sup>a</sup>, Franck Bassinot<sup>c</sup>, Tatiana Savranskaia<sup>b</sup>, Jean-Pierre Valet<sup>b</sup>, ASTER Team<sup>1</sup>

<sup>a</sup> CEREGE UM34, Aix Marseille Univ., CNRS, IRD, INRA, Coll France, Aix-en-Provence, France

<sup>b</sup> Institut de Physique du Globe de Paris, Sorbonne Paris-Cité, Université Paris Diderot, UMR 7154 CNRS, Paris, France

<sup>c</sup> LSCE, UMR8212, LSCE/IPSL, CEA–CNRS–UVSQ and Université Paris-Saclay, Gif-Sur-Yvette, France

## ARTICLE INFO

### Article history:

Received 20 December 2017

Received in revised form 22 February 2018

Accepted 24 February 2018

Available online xxxx

Editor: M. Frank

### Keywords:

authigenic  $^{10}\text{Be}/^9\text{Be}$  ratio  
geomagnetic dipole moment minimum  
Matuyama–Brunhes transition (MBT)  
geomagnetic polarity reversal  
marine isotope stage 19  
atmospheric  $^{10}\text{Be}$  production rates

## ABSTRACT

New high-resolution authigenic  $^{10}\text{Be}/^9\text{Be}$  ratio (Be-ratio) records covering the last geomagnetic reversal, i.e. the Matuyama–Brunhes transition (MBT), have been obtained and set on a time scale using benthic  $\delta^{18}\text{O}$  (*Cibicides wuellerstorfi*) records. The geographic distribution of the four studied sites allows global comparison between the North Atlantic, Indian and Pacific Oceans. All Be-ratio records contain a two-fold increase triggered by the geomagnetic dipole moment (GDM) collapse associated with the MBT. The stratigraphic position of the Be-ratio spike, relative to marine isotope stages, allows establishment of a robust astrochronological framework for the MBT, anchoring its age between 778 and 766 ka (average mid-peaks at 772 ka), which is consistent with all other available  $^{10}\text{Be}$ -proxy records from marine, ice and loess archives. The global  $^{10}\text{Be}$  atmospheric production doubling represents an increase of more than  $300 \text{ atoms m}^{-2} \text{ s}^{-1}$  that is compatible with the increased magnitude of atmospheric  $^{10}\text{Be}$  production obtained by simulations between the present GDM and a null-GDM. The minimum  $^{10}\text{Be}$ -derived GDM average computed for the 776–771 ka interval is  $1.7 \pm 0.4 \times 10^{22} \text{ Am}^2$ , in agreement with model simulations and absolute paleointensities of transitional lava flows.

© 2018 The Author(s). Published by Elsevier B.V. This is an open access article under the CC BY-NC-ND license (<http://creativecommons.org/licenses/by-nc-nd/4.0/>).

## 1. Introduction

The systematic coupling of polarity reversals with geomagnetic dipole moment (GDM) collapses constitutes the main entry for understanding fundamental mechanisms of the geodynamo (e.g. Amit et al., 2010). Magnetohydrodynamic models are beginning to provide insights into these mechanisms (Glatzmaier and Coe, 2015), but high-resolution and high-quality observations are vital to provide accurate constraints on long-term and rapid GDM variations. Paleomagnetic studies of the last geomagnetic reversal, i.e. the Matuyama–Brunhes transition (MBT), provide numerous records of dipole moment variations and virtual geomagnetic pole (VGP) paths of transitional states (e.g. synthe-

sis by Valet and Fournier, 2016), but several inconsistencies lead to conflicting interpretations on the geometry and chronology of the transitional field (Tauxe et al., 1996; Channell et al., 2010; Valet et al., 2012, 2016; Sagnotti et al., 2016; Mark et al., 2017; Channell, 2017). In sedimentary paleomagnetic records, the sources of such unconformities inconsistencies are multiple: i) multicomponent magnetizations (Roberts, 2015); ii) uncertainties or even ignorance about sediment magnetization lock-in processes (Roberts et al., 2013) and the influence of stronger post-transitional fields and (partial-) remagnetization/realignment of grains deposited in weak fields (Coe and Liddicoat, 1994; Simon et al., 2018); iii) signal smearing and averaging due to insufficient temporal resolution (Roberts and Winklhofer, 2004; Valet et al., 2016; Channell, 2017). Volcanic paleomagnetic records suffer from: i) spatial heterogeneity of thermoremanent magnetization acquisition along/across lava flow sections; ii) the influence of the magnetization of underlying lava flows on the local field recorded by the overlying flow while cooling (Vella et al., 2017); iii) discontinuous lava emission rates. Other biases that affect both types of records are due to regional

\* Corresponding author at: CEREGE UM34, Aix Marseille Univ., CNRS, IRD, INRA, Coll France, Aix-en-Provence, France.

E-mail address: [simon@cerege.fr](mailto:simon@cerege.fr) (Q. Simon).

<sup>1</sup> Georges Aumâtre, Karim Keddadouche.

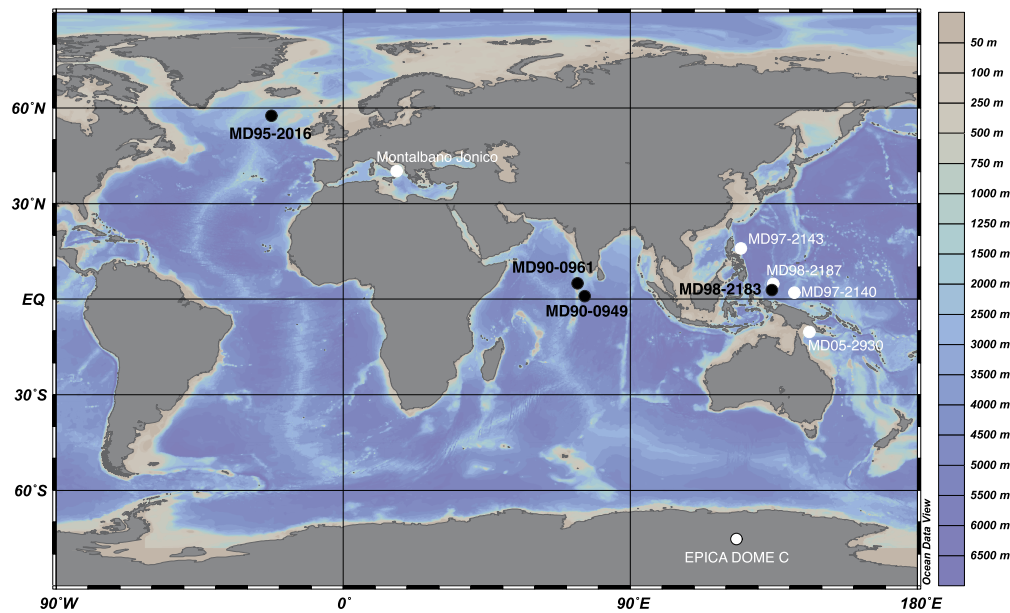


**Fig. 1.** Geographic locations of the four studied cores (black circles) along with Be-ratio and  $^{10}\text{Be}$ -flux from marine and glacial records discussed in the text (white circles). These references include: Montalbano Jonico (Simon et al., 2017); Epica Dome C (EDC) (Raisbeck et al., 2006); MD97-2140 (Carcaillet et al., 2003); MD97-2143 (Simon et al., 2018); MD05-2930 (Ménabréaz et al., 2014; Simon et al., 2016a), and MD98-2187 (Suganuma et al., 2010). (For interpretation of the colors in the figure(s), the reader is referred to the web version of this article.)

effects of non-dipole field sources (Leonhardt and Fabian, 2007; Amit et al., 2010) and chronological uncertainties in astrochronological, radiometric and other dating calibrations (e.g. Lisiecki and Raymo, 2009; Jicha et al., 2016; Niespolo et al., 2017). All of these factors restrict the reliability of our understanding of the morphology (intensity and direction) and chronology (timing and duration) of transitional fields.

A complementary and independent method to reconstruct the GDM variation is provided by reconstruction of time variations of the atmospheric production of the cosmogenic nuclide Beryllium-10 ( $^{10}\text{Be}$ ). Pioneering studies showed that cosmogenic nuclide production is inversely proportional to the GDM (e.g. Lal and Peters, 1967). This inverse relationship was later demonstrated and quantified (e.g. Kovaltsov and Usoskin, 2010 and references therein). The most detailed  $^{10}\text{Be}$  records from marine sediments, loess, or ice cores also document large  $^{10}\text{Be}$  overproduction episode that corresponds to the dipole intensity collapse at the MBT (Raisbeck et al., 1985, 2006; Carcaillet et al., 2003, 2004; Suganuma et al., 2010; Zhou et al., 2014; Ménabréaz et al., 2014; Valet et al., 2014; Simon et al., 2017, 2018). Recent studies by Simon et al. (2016a, 2018) further strengthen evidence for the systematic occurrence of  $^{10}\text{Be}$  overproduction episodes associated with geomagnetic dipole minima linked to polarity reversals and excursions over the last 2 Ma. This supports the use of  $^{10}\text{Be}$  for reconstructing accurate GDM changes.

Here, we present new authigenic  $^{10}\text{Be}/^9\text{Be}$  ratio (Be-ratio hereafter) and benthic  $\delta^{18}\text{O}$  results across the MBT interval from three marine sediment cores collected in the Indian, Pacific, and North Atlantic Oceans, which are integrated with published results from core MD90-0961 (Valet et al., 2014). The 2-cm sampling resolution allows interpretation and comparison of Be-ratio variations during the last reversal from these four distant sites with unprecedented high-resolution. The  $\delta^{18}\text{O}$  records permit comparison of the stratigraphic positions of Be-ratio variations and enable development of a reliable astrochronological framework for the MBT. Robust reconstruction of dipole moment variations over the last geomagnetic reversal provides new constraints, independent from paleomagnetism, which assists with understanding paleo-records and geodynamo simulations.

## 2. Materials and methods

### 2.1. Core locations and sampling strategy

The marine sediment cores studied were retrieved using the Calyppo coring system on board the R/V Marion-Dufresne from the Indian (MD90-0949 and MD90-0961), Pacific (MD98-2183), and North Atlantic (MD95-2016) Oceans (Fig. 1 and Table 1). They were sampled using u-channels and individual 8 cm<sup>3</sup> cubic plastic boxes for paleomagnetic measurements. The cubes were later subsampled for Be and  $\delta^{18}\text{O}$  measurements following completion of the paleomagnetic analyses, which ensures reliable depth correlations between paleomagnetic and geochemical results. Magnetic measurements performed on u-channel and individual samples indicate the depth of the MBT in cores MD98-2183 (Yamazaki and Oda, 2005; Valet et al., 2016), MD90-0961 (Valet et al., 2014), and MD90-0949/MD95-2016 (Valet et al., 2016). We used these paleomagnetic results to sample at high-resolution over stratigraphic intervals that correspond to the MBT in each core. Be results from core MD90-0961 were presented by Valet et al. (2014) and corrected by Simon et al. (2016a).

### 2.2. Oxygen isotopes

Stable oxygen isotopic compositions were measured on the benthic foraminifera species *Cibicides wuellerstorfi* (>150  $\mu\text{m}$  size-fraction) at  $\sim 2$  to 4 cm stratigraphic intervals. Analyses were performed with VG-Optima or Elementar Isoprime dual-inlet gas mass spectrometers at the Laboratoire des Sciences du Climat et de l'Environnement (LSCE). All results are expressed as  $\delta^{18}\text{O}$  vs. VPDB (in ‰) with respect to NBS 19 standard. The internal analytical reproducibility determined from replicate measurements of a carbonate standard is  $\pm 0.05\%$  ( $1\sigma$ ).

### 2.3. Australasian microtektites

Microtektite analysis was carried out on cores MD90-0961, MD90-0949, and MD98-2183 to detect the thickness of the sedimentary mixed layer and to provide an independent stratigraphic

**Table 1**  
Core locations and average sedimentation rates.

Cores	Latitude/longitude (°)	Water depth (m)	Average sedimentation rate (cm/ka)	# Be samples
MD98-2183	2°00.82'N/135°01.26'E	4388	2.0 ± 0.6	138
MD95-2016	57°42.46'N 29°25.44'W	2318	3.1 ± 1.0	182
MD90-0949	2°06.90'N 76°06.50'E	3600	2.0 ± 0.5	124
MD90-0961	5°03.71'N 73°52.57'E	2446	4.2 ± 0.6	116
MD97-2143 <sup>a</sup>	15°87'N/124°65'E	2989	1.1 ± 0.3	51

Average sedimentation rates and sample numbers are from the ~700–850 ka age interval in each core (see data in the supplementary material, Tables S1–S4).

<sup>a</sup> Data from Simon et al. (2018).

marker. These microtektites were produced after a meteoritic impact that preceded the MBT by 12–15 ka, and are found in marine sediments throughout much of the Indian Ocean and in marginal seas of the western Pacific Ocean (Schneider et al., 1992; Lee and Wei, 2000; Sukanuma et al., 2011; Valet et al., 2014). Following the procedure established by Schneider et al. (1992), sediment samples were treated with 0.1 M HCl, a 20% H<sub>2</sub>O<sub>2</sub> solution, and a 5% sodium hexametaphosphate solution to remove carbonate and residual organics, and to aid disaggregation. The samples were wet-sieved and the >100 μm fraction was examined visually using a binocular microscope. Only objects identified unambiguously as microtektites were counted.

#### 2.4. Beryllium principles and measurements

The exchangeable-<sup>10</sup>Be concentration measured in sediments, or authigenic <sup>10</sup>Be hereafter, corresponds to the fraction that is adsorbed or chemically precipitated onto settling particles. It primarily depends on <sup>10</sup>Be atmospheric production rate but is also affected by secondary environmental components (oceanic transport processes or detrital input changes). These secondary environmental components are minimized/removed by using authigenic <sup>9</sup>Be as a normalizer (Bourlès et al., 1989) in most records, which makes it possible to infer geomagnetic paleointensity variations from the Be-ratio (Simon et al., 2016a and references therein).

Authigenic Be isotopes analyses were carried out at the CEREGE National Cosmogenic Nuclides Laboratory (LN2C), France. A total of 444 samples were collected from cores MD90-0949, MD95-2016, and MD98-2183 over the ~700–850 ka age interval with variable sampling resolution ranging from 10 to 1 cm. These results complete previous Be-measurements performed using the same method on core MD90-0961 (Table 1). An average 2-cm sampling interval is attained within the MBT interval in each core. The samples have been treated according to the chemical procedure established by Bourlès et al. (1989) and revised by Simon et al. (2016b). Authigenic <sup>10</sup>Be and its stable isotope <sup>9</sup>Be were extracted from ~1 g dry samples by soaking them in a 20 ml leaching solution (0.04 M hydroxylamine (NH<sub>2</sub>OH–HCl) and 25% acetic acid) at 95 ± 5 °C for 7 h. A 2 ml aliquot of the resulting leaching solution was sampled for measurement of the natural <sup>9</sup>Be concentration using a graphite-furnace Atomic Absorption Spectrophotometer (AAS) with a double beam correction (Thermo Scientific ICE 3400<sup>®</sup>). The remaining solution was spiked with 300 μl of a 9.8039 × 10<sup>-4</sup> g g<sup>-1</sup> <sup>9</sup>Be-carrier before Be-purification by chromatography to determine accurately <sup>10</sup>Be sample concentrations from accelerator mass spectrometer (AMS) measurements of <sup>10</sup>Be/<sup>9</sup>Be ratios at the French AMS national facility ASTER (CEREGE). <sup>10</sup>Be sample concentrations were calculated from the measured spiked <sup>10</sup>Be/<sup>9</sup>Be ratios normalized to the BeO STD-11 in-house standard (1.191 ± 0.013 × 10<sup>-11</sup>) (Braucher et al., 2015) for cores MD95-2016 and MD98-2183; and to the NIST 4325 Standard Reference Material (2.79 ± 0.03 × 10<sup>-11</sup>) (Nishiizumi et al., 2007) for cores MD90-0961 and MD90-0949. Authigenic <sup>10</sup>Be concentrations are decay-corrected using the <sup>10</sup>Be half-life ( $T_{1/2}$ )

of 1.387 ± 0.012 Ma (Chmeleff et al., 2010; Korschinek et al., 2010).

### 3. Results and interpretations

Results are plotted in Fig. 2 as a function of the corrected depths of each core, with δ<sup>18</sup>O and microtektite in the upper panel, and <sup>10</sup>Be and <sup>9</sup>Be concentrations and Be-ratios in the middle and lower panels, respectively, and are listed in Supplementary Material (Tables S1 to S4). The polarity change associated with the MBT is marked by the reversal angle (lower panel of Fig. 2) that defines the angular deviation between the measured magnetic vector and the direction of the axial dipole field at the site latitude (Valet et al., 2016). It describes the variability of the local magnetic field vector without any *a-priori* assumption regarding the field geometry inherent to the VGP. The transitional interval corresponds to the sediment thickness between angular deviations of 30° and 150°.

The benthic *Cibicides wuellerstorfi* δ<sup>18</sup>O data vary between ~3.2 and 4.7‰ at the North Atlantic site (MD95-2016) and oscillate between ~2.4 and 4.2‰ at the Indian (MD90-0949 and MD90-0961) and western Pacific sites (MD98-2183) (Fig. 2). Glacial–interglacial cycles are labeled according to the nomenclature proposed by Railsback et al. (2015). A sharp decrease of ~1.2 to 1.5‰ characterizes termination 9 (the deglaciation between marine isotope stage (MIS) 20 and 19c) at each site, while the MIS 19c–MIS 18e transition is more gradual, with secondary oscillations at sub-stages MIS 19a–b. The amplitude of glacial–interglacial δ<sup>18</sup>O transitions corresponds to those observed in the LR04 global benthic stack (~1.2‰), which is indicative of recording of a reliable global ice volume signature (Lisiecki and Raymo, 2005). The record from core MD90-0961 is limited to the MIS 20–19a interval and has been completed by *Cibicides wuellerstorfi* δ<sup>18</sup>O data from sister core MD90-0963 retrieved at the same location (Bassiot et al., 1994). Massive carbonate dissolution occurs in core MD98-2183 at the MIS 19 level, which complicates robust interpretation apart from primary glacial–interglacial oscillations. Furthermore, the rapid δ<sup>18</sup>O increase at 3040 cm toward a value close to glacial ones together with the following 40 cm data gap precludes identification of any MIS 19 sub-stages in this core.

A microtektite layer is identified in cores MD90-0961 (Valet et al., 2014) and MD90-0949, but is not observed in core MD98-2183. The maximum concentration coincides with the onset of termination 9 in both cores, and is followed by a progressive decrease over 23 and 26 cm in core MD90-0961 and MD90-0940, respectively. This reflects smearing induced by bioturbation in the surficial mixing layer (Fig. 2). Similar 20–25 cm depth ranges between the maximum concentration and disappearance of microtektites have been observed at sites ODP 758B and 769A (Schmidt et al., 1993) and MD97-2142 (Lee and Wei, 2000), while it is 15–20 cm in cores MD97-2187 (Sukanuma et al., 2011) and MD97-2143 (Lee and Wei, 2000). Microtektite concentrations in these two cores are, however, lower than that at the other sites. Although limited, this site comparison suggests a first-order influence of the initial microtektite

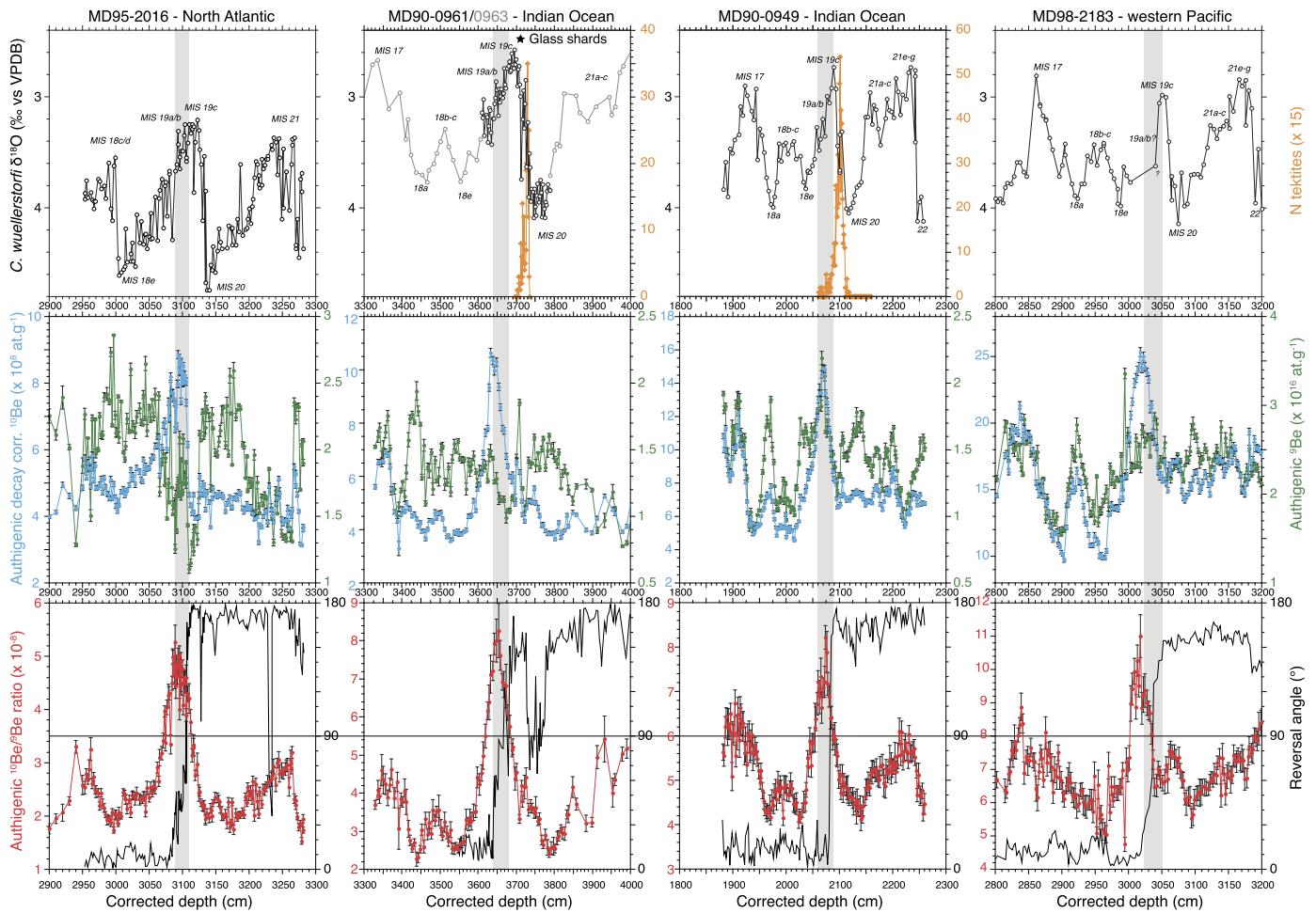


**Fig. 2.** Oxygen and beryllium isotope results. The benthic *Cibicides wuellerstorfi*  $\delta^{18}\text{O}$  records and microtektite distributions (orange) are represented in the upper panel. Marine isotopic stage (MIS) and sub-stage nomenclature is from Railsback et al. (2015). Authigenic  $^{10}\text{Be}$  (blue) and  $^9\text{Be}$  (green) concentration are shown in the middle panel. The Be-ratio (red) and reversal angle (black) for each core is represented in the lower panel. Note that different scales are used for the Be-data. The reversal angle (Valet et al., 2016) enables definition of the transitional field depth interval in each core. The grey bands highlight the transitional fields between full polarity states.

concentration, along with sedimentation rate, on the thickness of the mixing interval. This Australasian microtektite layer was also used to deconvolve the  $^{10}\text{Be}$  signal by Suganuma et al. (2011) and Valet et al. (2014), showing no stratigraphic displacement of the  $^{10}\text{Be}$  peak induced by bioturbation filtering. Volcanic glass shards (tephra) were also detected between depths of 3710 and 3713 cm in core MD90-0961 (Fig. 2) but were not geochemically studied here.

Authigenic  $^9\text{Be}$  concentrations vary from  $0.77$  to  $1.94 \times 10^{16}$  at  $\text{g}^{-1}$  in core MD90-0961 (mean value:  $1.34 \pm 0.22 \times 10^{16}$  at  $\text{g}^{-1}$ ) and from  $0.88$  to  $2.19 \times 10^{16}$  at  $\text{g}^{-1}$  (mean value:  $1.44 \pm 0.26 \times 10^{16}$  at  $\text{g}^{-1}$ ) in nearby core MD90-0949. In the two other cores, the higher authigenic  $^9\text{Be}$  concentrations vary over wider ranges, that is from  $1.45$  to  $3.36 \times 10^{16}$  at  $\text{g}^{-1}$  in core MD98-2183 (mean value:  $2.27 \pm 0.32 \times 10^{16}$  at  $\text{g}^{-1}$ ) and  $1.10$  to  $2.86 \times 10^{16}$  at  $\text{g}^{-1}$  in core MD95-2016 (mean value:  $1.92 \pm 0.37 \times 10^{16}$  at  $\text{g}^{-1}$ ). In the North Atlantic Ocean core MD95-2016, authigenic  $^9\text{Be}$  variations seem to be influenced by the glacial-interglacial pattern.  $^9\text{Be}$  concentration maxima coincide with glacial  $\delta^{18}\text{O}$  values, which suggests that  $^9\text{Be}$  delivery at the location is influenced by denudation rates and clastic inputs (e.g. Simon et al., 2016b) and/or hydrographic changes (water flow speed and northern source water; Kleiven et al., 2011). In core MD90-0949, on the contrary,  $^9\text{Be}$  maxima occur during interglacial MIS 19, while in nearby MD90-0961 core no particular  $^9\text{Be}$  trend is observed during MIS 19, which suggests different  $^9\text{Be}$  oceanic pathways for these neighboring cores situated at differ-

ent water depths (Table 1). These relationships are likely related to i) sediment provenance changes influenced by oceanic circulation and ii) water mass stratification changes. The  $^9\text{Be}$  record of core MD98-2183 is characterized by minor oscillations between MIS 21 and 19 and two successive minima within the MIS 18b–c interval and at the MIS 17–18a transition.

The authigenic  $^{10}\text{Be}$  concentrations (decay-corrected) vary from  $3.30$  to  $10.64 \times 10^8$  at  $\text{g}^{-1}$  and  $4.56$  to  $14.89 \times 10^8$  at  $\text{g}^{-1}$  in cores MD90-0961 (mean value:  $5.14 \pm 1.57 \times 10^8$  at  $\text{g}^{-1}$ ) and MD90-0949 (mean value:  $7.52 \pm 2.20 \times 10^8$  at  $\text{g}^{-1}$ ), respectively. The authigenic  $^{10}\text{Be}$  concentrations in core MD95-2016 (North Atlantic) are similar to the authigenic  $^{10}\text{Be}$  concentration values of core MD90-0961, ranging from  $3.13$  to  $8.85 \times 10^8$  at  $\text{g}^{-1}$  (mean value:  $5.15 \pm 1.31 \times 10^8$  at  $\text{g}^{-1}$ ). In core MD98-2183 from the Pacific Ocean, the authigenic  $^{10}\text{Be}$  concentrations are nearly two times higher and are distributed over a wider range, that is from  $9.71$  to  $25.34 \times 10^8$  at  $\text{g}^{-1}$  (mean value:  $15.82 \pm 3.42 \times 10^8$  at  $\text{g}^{-1}$ ). The main feature in all studied cores is the large increase in  $^{10}\text{Be}$  concentration compared with the surrounding intervals in MIS 19a–b (Fig. 2). A secondary  $^{10}\text{Be}$  peak is also observed during MIS 17 while a minor  $^{10}\text{Be}$  increase is observed during MIS 18a at each site.

In cores MD90-0961 and MD90-0949, Be-ratios vary from  $2.26$  to  $8.27 \times 10^{-8}$  (mean value:  $3.93 \pm 1.36 \times 10^{-8}$ ) and  $4.07$  to  $8.22 \times 10^{-8}$  (mean value:  $5.19 \pm 0.84 \times 10^{-8}$ ), respectively. In core MD98-2183, the Be-ratio varies from  $4.75$  to  $11.01 \times 10^{-8}$  (mean

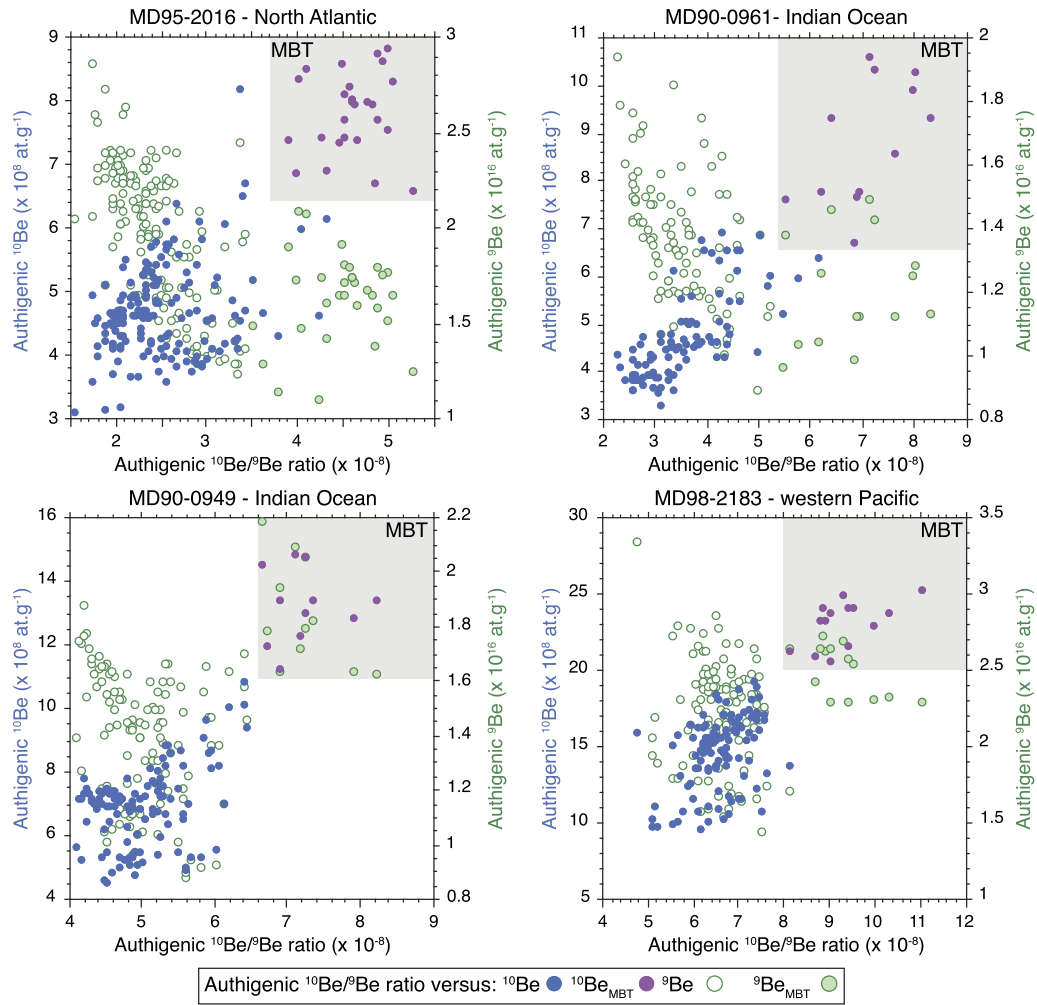


**Fig. 3.** Authigenic Be-ratios versus  $^{10}\text{Be}$  and  $^9\text{Be}$  concentrations. The grey-shaded area represent values within the MBT interval. See Table S5 for correlation coefficients.

value:  $6.96 \pm 1.05 \times 10^{-8}$ ) and in core MD95-2016 from  $1.53$  to  $5.26 \times 10^{-8}$  (mean value:  $2.78 \pm 0.89 \times 10^{-8}$ ). These average Be-ratios correspond to different ocean basin averages estimated by von Blanckenburg and Bouchez (2014) from modern sea water and deep ocean surface sediment Be concentrations, therefore supporting complete homogenization of both Be isotopes in the water column (see Wittmann et al., 2017). The significant relationship between the long-term average Be-ratio and  $^{10}\text{Be}$  with site water depths ( $r > 0.9$ ) favors higher scavenging of  $^{10}\text{Be}$  at deeper sites likely resulting from longer sinking particle residence times, a higher  $^{10}\text{Be}$  reservoir at these sites, and/or associated with carbonate compensation depth that could have contributed to increase the relative concentrations of both Be isotopes at site MD98-2183. A negative correlation between sedimentation rate and Be-ratio ( $r = -0.7$ ) also suggests higher Be contents at slow deposition sites. Except for these long-term average Be-ratio features between cores, the main Be-ratio change in all cores is characterized by a doubling in MIS 19a–b compared with surrounding intervals.

In three of the four cores, the main Be-ratio peak coincides with transitional paleomagnetic directions that identify the Matuyama–Brunhes polarity transition (dark grey banding in Fig. 2). In core MD97-2183, an 18-cm stratigraphic offset between the Be-ratio mid-peak and the polarity reversal is observed. Such offsets have been identified in clayey and carbonate sedimentary sequences from the Western Pacific Ocean (MD97-2140, Carcaillet et al., 2003; MD97-2143, Suganuma et al., 2010; Simon et al., 2018) and from the Northeast Atlantic Ocean (MD95-2040, MD95-2042,

Carcaillet et al., 2004; MD04-2811, Ménabréaz et al., 2011). With thicknesses of a few cm to several tens of cm, they are compatible with the effects of post-depositional magnetization lock-in (e.g. Roberts et al., 2013) as the residence time of dissolved Be isotopes in the oceans (200 to 700 years at studied sites; von Blanckenburg et al., 1996) can produce at best depth offsets of 0.5 to 2 cm, depending on sedimentation rate of each site.

The first order Be-ratio peak in all studied cores can, therefore, be related to enhanced cosmogenic nuclide production produced by the geomagnetic dipole minimum associated with the last polarity reversal. Such a Be-ratio, or  $^{10}\text{Be}$ -flux, doubling has been observed in marine sediments and ice core records at the time of the MBT reversal and during the main dipole minima linked to reversals and excursions of the late Matuyama chron and to excursions of the Brunhes chron (e.g. Raisbeck et al., 1985, 2006; Frank et al., 1997; Carcaillet et al., 2003; Suganuma et al., 2010; Ménabréaz et al., 2014; Horiuchi et al., 2016; Simon et al., 2016a, 2018 and references therein).

Significant positive correlation coefficients between  $^{10}\text{Be}$  and the Be-ratio ( $r = 0.77$  to  $0.90$ ) support a strong control of  $^{10}\text{Be}$  variations on the Be-ratio over the studied interval (Fig. 3 and Table S5). No significant correlation between  $^9\text{Be}$  and Be-ratio is noted, except in cores MD90-0961 and MD95-2016, where  $r$  values around  $-0.5$  suggest that the normalization procedure did not fully remove possible environmental imprints. A principal component analysis on the four Be-ratio series provides a PC1 that explains 88% of the total variance (Fig. 4C). Three Be-ratio series

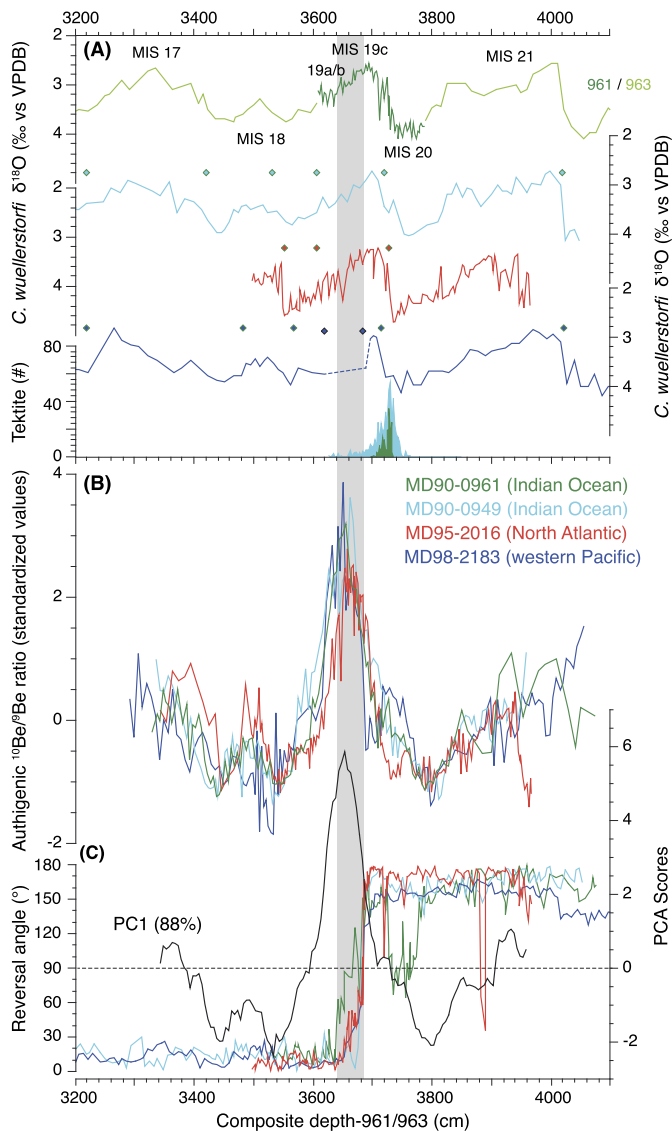


**Fig. 4.** Results plotted on a common depth scale. (A)  $\delta^{18}\text{O}$  records synchronized to a common depth scale (MD90-961/963 as a target) using minimal tie points numbers (indicated by diamonds). (B) Be-ratios from each core standardized over the same composite depth for the same time period, i.e. 700–850 ka. (C) Scores of the first principal component (PC1 explains 88% of the variance) from a principal component analysis on the four Be-ratio series studied, and reversal angles defining the transitional field depth intervals in each core (Valet et al., 2016). The grey band highlights the transitional fields between full polarity states, as indicated by reversal angles between  $30^\circ$  and  $150^\circ$ .

are highly correlated ( $r > 0.92$ ) with PC1, which supports a major common forcing by dipole moment changes. The fact that the MD95-2016 Be-ratio record presents a slightly lower correlation with PC1 ( $r = 0.82$ ) is probably due to the secondary environmental influence or a weak stratigraphic offset within the uncertainty range (see below; Fig. 4B–C).

If the data associated with the MBT dipole minimum are removed, the correlation between  $^{10}\text{Be}$  and Be-ratio decreases significantly, while the correlation between  $^9\text{Be}$  and Be-ratio data increases. This further confirms that the  $^{10}\text{Be}$  produced during the geomagnetic dipole minimum interval provides the main constraint on the Be-ratio variation and its dependence on the dipole moment value. The MBT is, therefore, identified accurately by cosmogenic  $^{10}\text{Be}$  nuclide enhancements in natural archives (grey shaded area in Fig. 3). Furthermore, and despite traces of possible environmental components in the Be-ratio of two of the four cores

studied, the amplitude of the Be-ratio increase at the MBT remains constant between each site, once standardized (z-score) over the same composite depth interval (representing the 700 to 850 ka age interval) (Fig. 4B). All of these observations confirm the reliability of the  $^9\text{Be}$  normalization method to provide a robust identification of the geomagnetic dipole moment collapse associated with the MBT in each studied core (Fig. 4B).

#### 4. Common depth scale and chronological framework

The chronological framework required to globally assess the age and duration of the MBT is obtained from radiometric dating and/or astrochronological calibrations (e.g. Coe et al., 2004; Channell et al., 2010). These methods provide reliable solutions but contradictory results, and lead to disputed ages (see Mark et al., 2017 and comment by Channell and Hodell, 2017). The chronology of the present synthetic record was constructed by applying an orbital tuning on the benthic oxygen isotope records. This strategy provides a relative chronology with maximum age errors of  $\pm 5$  ka for ages around the MBT interval due to uncertainties on delays between the insolation signal and the global response of ice caps (Lisiecki and Raymo, 2005).

The two-steps approach used in this study is described as follows. First, all records were placed on a common depth scale by correlating high-resolution  $\delta^{18}\text{O}$  benthic records (*Cibicides wuellerstorfi*) (Fig. 4A), assuming global synchronicity between benthic  $\delta^{18}\text{O}$  signals (see below). Site MD90-0961/0963 (Indian Ocean), which has been studied extensively for paleomagnetism and oxygen isotope geochemistry (Bassinot et al., 1994; Valet et al., 2014, 2016), was selected as the common reference target. Depth scales for all other records were rescaled using a minimum number of tie-points to avoid accordion-like stratigraphic shifts (Fig. 4A). This strategy leads to a clear and robust core-to-core correlation and permits accurate assessment of the position of Be-ratio peaks associated with the MBT versus climatostratigraphic markers (Fig. 4B). In core MD98-2183, benthic foraminifera dissolution within MIS 19 (dashed line in Fig. 4A) hampers use of the isotopic signal for providing independent constraints outside of the primary glacial/interglacial oscillations. The Be-ratio peak limits associated with the MBT were, therefore, used to adjust the depth scale, providing better alignment that is not independent of Be measurements. In cores MD90-0961 and MD90-0949, perfect alignment of the microtektite peak at 3730 cm (common depth) provides a robust stratigraphic marker, independent of the adjustment strategy (Fig. 4A). Moreover, all Be-ratio peaks and transitional reversal angle paths are located between  $\sim 3620$  and  $3680$  cm and between  $\sim 3640$  and  $3690$  cm, respectively (Fig. 4B–C). Such successful alignment of independent proxy records is consistent with the assumption of global average synchronicity of benthic  $\delta^{18}\text{O}$  records, within uncertainty limits, which supports our strategy. Chronological offsets between benthic series produce stratigraphic misalignments by 2 to 4 ka between oceanic basins at glacial terminations (Lisiecki and Raymo, 2009), but since they mainly concern glacial terminations, they have minor impact on astrochronological dating of the MBT within MIS 19.

Second, we derived a common chronological framework by tuning fine-scale  $\delta^{18}\text{O}$  features from each record placed on a common depth scale, with the global benthic  $\delta^{18}\text{O}$  LR04 stack of Lisiecki and Raymo (2005) (Fig. 5). In parallel, tuning of individual  $\delta^{18}\text{O}$  records on their own depth scales with the LR04 stack was also performed to evaluate uncertainties in the matching procedure. Average age deviations between the two derived chronologies (common and individual depths) lie between 0.4 and 2 ka, i.e. less than the  $\pm 5$  ka uncertainty associated with the LR04 stack in the 0–1 Ma time interval (Lisiecki and Raymo, 2005). This new chronological reconstruction provides an age of 793–794 ka for the Australasian

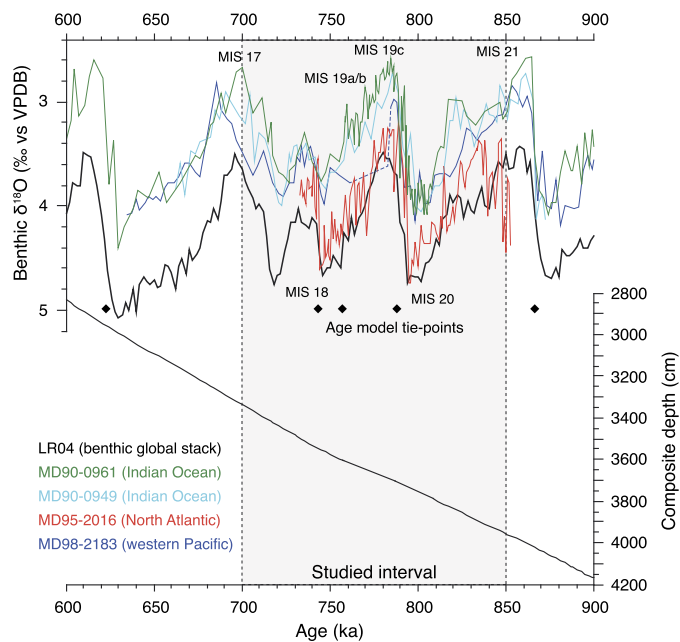


**Fig. 5.** Chronostratigraphy for the records studied here. Benthic foraminifera *Cibicides wuellerstorfi* oxygen isotope stratigraphy from all cores (see legend) have been tuned to the benthic LR04 global stack (Lisiecki and Raymo, 2005) to derive a common astrochronological framework.

microtektite layer identified in cores MD90-0961 and MD90-0949. This age lies between two  $^{40}\text{Ar}/^{39}\text{Ar}$  ages obtained for this layer: a maximum age at  $799.2 \pm 3.8$  ka (Smit et al., 1991) and a minimum age at  $786 \pm 2$  ka (Mark et al., 2017). Furthermore, volcanic glass shards (tephra) detected in the 3710–3713 cm depth interval in core MD90-0961 lie at ca 789–790 ka. This is indistinguishable from the astronomically tuned age of Ash D at ODP Site 758:  $788.0 \pm 2.2$  ka (Lee et al., 2004) and is coherent with two distinct eruptions from the Toba volcano (OTTA and OTTB) that are dated radiometrically at  $792.4 \pm 0.6$  ka and  $785.6 \pm 0.8$  ka (Mark et al., 2017).

The chronological coherency between the astronomical age model and independently dated events confirms the reliability of our age framework. The new chronological framework allows accurate computation of sedimentation rates for the MBT interval in all studied cores (Table 1). The 2-cm sampling spacing then implies an integrated time interval ranging from 0.5 to 1 ka. Adding the slight signal smoothing induced from bioturbation and oceanic Be residence time, this sampling spacing provides millennial resolution, which is the finest resolution possible from cores with such low to moderate sedimentation rates. A duration of 30 to 32 ka for MIS 19 is deduced from sedimentation rates, in agreement with other estimates (33 ka, Tzedakis et al., 2012; 34 ka, Giaccio et al., 2015). Similarly, an average duration of 11 ka estimated for MIS 19c is also coherent with records from Montalbano Jonico (11.2 ka, Simon et al., 2017), Sulmona paleolake (10.8 ka, Giaccio et al., 2015), and the North Atlantic Ocean (10.5–12.5 ka, Tzedakis et al., 2012). It is worth noting that average sedimentation rates computed for the 700–850 ka interval (Table 1) are 12 to 55% lower than previous estimates by Valet et al. (2016), which considered the complete sediment thickness between core tops and the MBT. By doing so, these estimates neglected the significant stretching effect imposed by the Calypso corer on the upper 10–15 meters of the first generation of *Marion Dufresnes* cores that has been demonstrated by anisotropy of magnetic susceptibility measurements (Thouveny et al., 2004).

## 5. Global $^{10}\text{Be}$ overproduction episode at the time of the MBT

### 5.1. General comments

The occurrence of a single large Be-ratio peak interval is demonstrated in all studied cores (Fig. 4B). Their alignment/coincidence in the common stratigraphic/chronological framework indicates that they result from the same global  $^{10}\text{Be}$  overproduction episode triggered by the GDM collapse linked to the MBT (Fig. 4C). After standardization, these Be-ratio peaks have the same amplitude at all sites, which confirms the global homogenization and deposition of atmospheric  $^{10}\text{Be}$  produced during the MBT. This is further confirmed by the high correlation of each Be-record with the first principal component PC1 (see section 3) that explains 88% of the variance of the Be-ratio series with a broad peak with highest scores at 766–778 ka (mid peak at  $\sim 772$  ka) (Fig. 6). The fact that this Be-ratio peak coincides with the minimum of summer insolation linked with the end of interglacial MIS 19c (Fig. 6) allows fixing of the age of the MBT between 770 and 778 ka. Using June 21 as a reference instead of mean summer insolation accounts for a maximum 2 ka age shift toward older ages. This age range is compatible with: 1) astronomical calibration of paleomagnetic records (e.g. Tauxe et al., 1996; Channell et al., 2010; Channell, 2017); 2) radiometric dating of the transitional Haleakala lava flow ( $776.0 \pm 2.0$  ka; Coe et al., 2004), which has been recently revised to  $772.0 \pm 2.0$  ka (Singer et al., 2017) using a new generation of multi-collector mass spectrometers (Jicha et al., 2016); 3) radiometric dating at  $774.1 \pm 0.9$  ka of a tephra layer in the Montalbano Jonico section (Nomade et al., in revision) within the Be-ratio peak associated with the MBT (Simon et al., 2017) (Fig. 6); 4) the age of the VGP midpoint horizon in the Chiba record calculated at  $770.9 \pm 7.3$  ka from the U-Pb zircon age of a tephra layer deposited immediately below (Okada et al., 2017); and 5) a weighted average age of  $779 \pm 7.5$  ka calculated by Mark et al. (2017) from the four transitional lava flows presented by Singer et al. (2005). Furthermore, our new Be-ratio records are remarkably similar to all currently available Be-ratio MBT records from marine sediment sequences (Fig. 6). Finally, the duration of the  $^{10}\text{Be}$  overproduction episode deduced from our new Be-ratio records (766–778 ka) is similar to that measured in the EPICA Dome C (EDC) ice record (Raisbeck et al., 2006) when set on the AICC2012 chronology (Bazin et al., 2013) (Fig. 6).

All data currently available from different geological reservoirs, thus, confirm the global stratigraphic/chronologic coherence of the  $^{10}\text{Be}$  overproduction interval associated with the MBT (Fig. 6). All of these  $^{10}\text{Be}$  data provide compelling arguments in favor of the younger age scenario for the MBT (i.e.  $\sim 772$  ka) despite the fact that some recent paleomagnetic and radiometric dating results support an overall older age at  $783.4 \pm 0.6$  ka (Mark et al., 2017). An accepted (common) definition of reversal boundary from the continuous transitional process, together with evaluation and comparison of the resolution of each proxy will help to better constrain their respective limitations (e.g. pDRM lock-in depths, astronomical and radiometric calibrations, environmental biases) and to reduce chronological disagreement (Valet et al., submitted).

The  $^{10}\text{Be}$  overproduction episode triggered by the MBT geomagnetic dipole minimum provides a globally synchronous marker that is useful for inter-correlation of ice-cores and continental (lacustrine and loess) and marine sediment records. The ages of GDM variations reconstructed either by paleointensity or by  $^{10}\text{Be}$  records should be the same in different parts of the globe. Therefore, dipole moment proxies should be more reliable than magnetization directions for providing dating and an inventory of paleomagnetic events such as excursions and reversals, mostly because

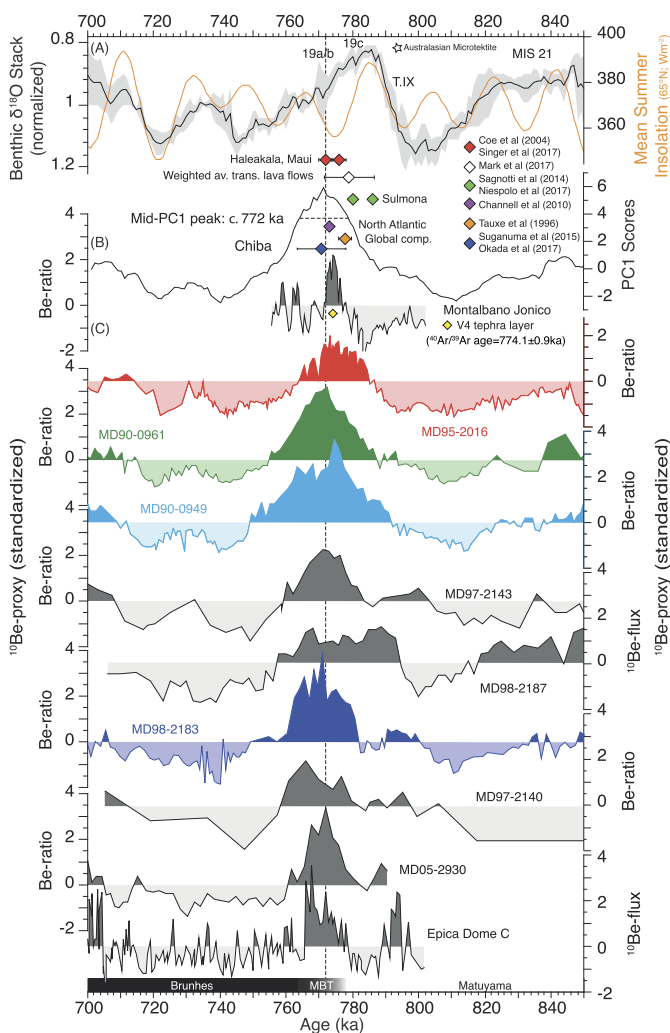


**Fig. 6.**  $^{10}\text{Be}$ -proxy comparison for the Matuyama–Brunhes transition. (A) Stack of the four benthic  $\delta^{18}\text{O}$  records and mean summer insolation at  $65^\circ\text{N}$  (Laskar et al., 2004). (B) Scores of the first principal component (PC1), which explains 88% of the total variance between all series. The age of c. 772 ka corresponds to the mid-PC1 peak. The colored diamonds correspond to radiometric estimates of MBT age (see references in the legend). (C) All  $^{10}\text{Be}$ -proxy records have been standardized over the same time interval and include: the Montalbano Jonico (Simon et al., 2017; Nomade et al., in revision); MD97-2143 (Simon et al., 2018); MD98-2187 (Suganuma et al., 2010); MD97-2140 (Carcaillet et al., 2003); MD05-2930 (Ménabréaz et al., 2014; Simon et al., 2016a); Epica Dome C (EDC) (Raisbeck et al., 2006).

rapid directional transitions are not adequately recorded in low-to-moderate sedimentation rate cores (Roberts and Winkhofer, 2004; Valet et al., 2016; Channell, 2017) and stratigraphic/temporal offsets, such as pDRM effects, lead to chronological errors and misinterpretations. Cosmogenic signatures of reversals or excursions should, thus, be investigated systematically together with paleomagnetic signatures, especially when hypotheses of paleomagnetic field – paleoclimate connections are discussed.

Despite overall agreement between paleomagnetic and cosmogenic expressions of dipole field variations, unresolved differences appear or persist, which gives rise to methodological or theoretical discussions. The best example is the occurrence of a paleointensity minimum reported before the MBT in some marine sediments and lava flows, which suggests the occurrence of a precursor event prior to the MBT (e.g. Hartl and Tauxe, 1996). On the one hand, Be-ratio records from the North Atlantic Ocean (MD95-2016), Mediterranean Sea (Montalbano Jonico; Simon et al., 2017), and Indian Ocean (MD90-0961 and MD90-0949) do not document such an

occurrence (Fig. 6), but on the other hand, Be-ratio records from the Pacific Ocean and Antarctica contain weak  $^{10}\text{Be}$  enhancements prior to the MBT. In core MD98-2183, a small Be-ratio increase before the MBT is coherent with a  $^{10}\text{Be}$ -flux maximum observed in the nearby core MD98-2187 (Suganuma et al., 2010). In core MD05-2930, such a signature can be identified at the core bottom (Fig. 6). In cores MD97-2143 (Simon et al., 2018) and MD97-2140 (Carcaillet et al., 2003), the MBT is preceded by a two steps enhancement. The Antarctic EDC ice core record also contains a  $^{10}\text{Be}$  flux enhancement prior to the MBT signature (Raisbeck et al., 2006). However, several critical points are evident for these studies. For example, 1) the exact  $^{10}\text{Be}$  signature of the precursor in the EDC record can be questioned based on glaciological constraints induced by high pressures at the bottom (below 3000 m deep) of the EDC core (Simon et al., 2016a), 2) a large fraction of the high  $^{10}\text{Be}$ -fluxes attributed to the precursor by Suganuma et al. (2010) in core MD98-2187 likely results from strong environmental imprints during termination 9 (Simon et al., 2018). Moreover, the prominent minimum in the PISO-1500 stack is mainly induced by the IODP Site U1308 record (Channell et al., 2009) and is less obvious in other high-resolution North Atlantic records (see Fig. 10b in Xuan et al., 2016). The precursor may, therefore, result either from paleomagnetic biases or from still unquantified threshold effects of the dipole moment on magnetospheric shielding, and in turn on cosmogenic nuclide production, or from a mix of both. This question deserves to be clarified in new high-resolution paleomagnetic and cosmogenic records prior to drawing any firm geomagnetic conclusions.

## 5.2. Cosmogenic production models

The concurrent increase of  $^{10}\text{Be}$ -proxy (i.e. Be-ratio,  $^{10}\text{Be}$ -flux) observed in all records, including polar ice and mid-to-lower latitude marine sediment cores, at the MBT supports a global  $^{10}\text{Be}$  production rate increase. In order to estimate the amount of additional atmospheric  $^{10}\text{Be}$  produced during this dipole moment minimum, the Be-ratio GDM calibration of Simon et al. (2018) is compared with the global atmospheric  $^{10}\text{Be}$  production rate model of Poluianov et al. (2016) using a constant mean modulation potential of 650 MV (Fig. 7). Calibration of empirical versus theoretical production models allows the estimation of past global  $^{10}\text{Be}$  production rate changes (Fig. 7B). A normalized Be-ratio stack was constructed by compiling the individual Be-ratio records after even-spacing and averaging each series over 1 ka time windows. The global production rate of atmospheric  $^{10}\text{Be}$  changes calculated using this function and the Be-ratio stack increases two-fold from the base to the peak of the  $^{10}\text{Be}$  enhancement (Fig. 8). The periods that surround the main increase interval have average  $^{10}\text{Be}$  production rates similar to those measured in year 1980 by Monaghan et al. (1986) or simulated for modern periods (see box in Fig. 8 or Table 4 in Simon et al., 2016b).

Atmospheric  $^{10}\text{Be}$  production change computed during the dipole moment collapse of the last geomagnetic reversal that passes from  $\sim 300$  to  $>600$  atoms  $\text{m}^{-2} \text{s}^{-1}$  is a doubling of the average production outside the event, so that global  $^{10}\text{Be}$  atmospheric production increases by more than 300 atoms  $\text{m}^{-2} \text{s}^{-1}$  (Fig. 8). This is statistically comparable with the result ( $+272$  atoms  $\text{m}^{-2} \text{s}^{-1}$ ) of the theoretical model of Heikkilä et al. (2009) applied to present day production conditions (control run) and to the so-called “Laschamp-run”, a simulated  $^{10}\text{Be}$  production model for a zero geomagnetic field strength (Fig. 8). This comparison supports a global  $^{10}\text{Be}$  overproduction period induced by geomagnetic modulation at the MBT, and also indirectly confirms that stratospheric homogenization of  $^{10}\text{Be}$  is the controlling process for worldwide  $^{10}\text{Be}$  deposition flux. It also suggests that the  $^{10}\text{Be}$

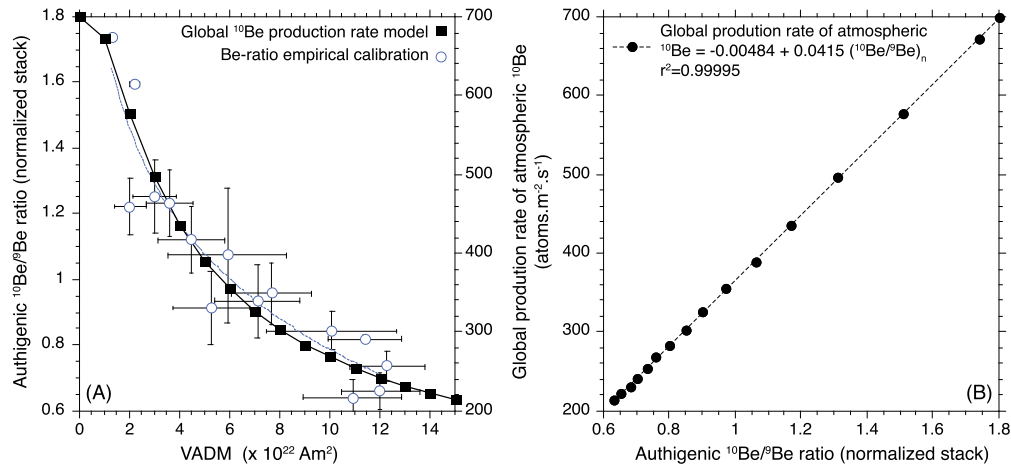


**Fig. 7.** Calibration of the authigenic  $^{10}\text{Be}/^9\text{Be}$  ratio in terms of  $^{10}\text{Be}$  global production rates. (A) Comparison between the empirical calibrations from Simon et al. (2018) and the global atmospheric  $^{10}\text{Be}$  production rate model of Poluianov et al. (2016). (B) Calibration curve.

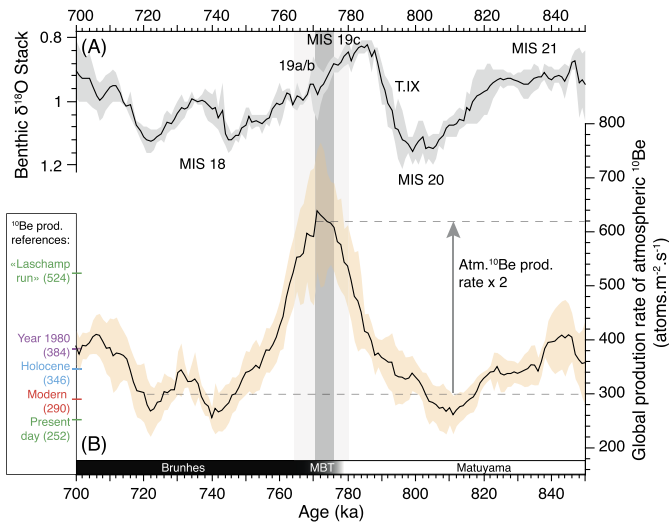


**Fig. 8.** Global production rate enhancement of atmospheric  $^{10}\text{Be}$  over the MBT. (A) Stack of the four benthic  $\delta^{18}\text{O}$  records. (B)  $^{10}\text{Be}$  global production rate curve obtained from the Be-ratio normalized stack of the four authigenic  $^{10}\text{Be}/^9\text{Be}$  ratio records calibrated to the global  $^{10}\text{Be}$  production model of Poluianov et al. (2016). Atmospheric  $^{10}\text{Be}$  production rates are compared to several references from numerical simulations and measurement estimates: i) global distribution (average area-weighted global flux) of Holocene  $^{10}\text{Be}$  fluxes from Heikkilä and von Blanckenburg (2015), ii) modern average global  $^{10}\text{Be}$  production rates from the Poluianov et al. (2016) model, iii) present day and “Laschamp run” (zero geomagnetic dipole) experiment outcomes of the Heikkilä et al. (2009) simulation, and iv) global average  $^{10}\text{Be}$  production measured and calculated for year 1980 by Monaghan et al. (1986).

production increase reaches a maximum plateau during the MBT (Fig. 7A).

## 6. GDM calibration of the $^{10}\text{Be}$ record and independent insight into field intensity changes

Determination and quantification of minimum value of GDM threshold required to trigger reversals and excursions are of fundamental importance for understanding geodynamo processes. Critical dipole moment values between  $\sim 1$  and  $2.5 \times 10^{22}$  Am $^2$ , i.e. 10 to 30% of the current dipole moment, have been suggested by simulations (e.g. Glatzmaier and Roberts, 1995; Buffett et al., 2013), paleomagnetic studies (e.g. Channell et al., 2009; Valet et al., 2005), and earlier cosmogenic nuclide production studies (Ménabréaz et al., 2012; Simon et al., 2016a). A combination of approaches is required to provide accurate values and to evaluate the relevance of input parameters for experimental and nu-

merical geodynamo simulations. Our normalized Be-ratio stack is calibrated using the global atmospheric  $^{10}\text{Be}$  production model of Poluianov et al. (2016) to produce a  $^{10}\text{Be}$ -derived GDM record (Fig. 7B). This approach differs from that used in earlier studies by Simon et al. (2016a, 2018), but relies on similar Be-ratios from marine sedimentary sequences to give comparable relative results (amplitude range) and only minor changes for quantitative reconstructions. The method also complements virtual axial dipole moment (VADM) and virtual dipole moment (VDM) estimates derived from paleointensity records that can be affected significantly by non-dipole components, particularly when the dipole vanishes.

A longstanding  $^{10}\text{Be}$ -derived GDM minimum that lasted 12 ka, from 778 to 766 ka, corresponds to the broad minimum in the PISO-1500 record (Fig. 9). This period is characterized by values below  $2.2 \times 10^{22}$  Am $^2$  (i.e.  $\sim 35\%$  of the time-averaged VADM within the 700–850 ka period or  $\sim 30\%$  of the current VADM). The sharper field recovery observed in the PISO-1500 stack compared to the  $^{10}\text{Be}$ -derived record might result either from a smoothing of the Be-ratio signal, or an overprint from the high intensity post-transitional field on magnetic grains deposited during the low intensity MBT interval (Coe and Liddicoat, 1994; Fig. 9). The fact that no similar offset is observed elsewhere supports this last interpretation, but it needs to be carefully scrutinized for other paleointensity minima. The average of minimum  $^{10}\text{Be}$ -derived GDM values between 776 and 771 ka ( $1.7 \pm 0.4 \times 10^{22}$  Am $^2$ ) is the same as the minimum value for transitions in numerical simulations (e.g. Glatzmaier and Roberts, 1995; Buffett et al., 2013; Wicht and Meduri, 2016). It is also the same value as that derived from calibrated RPI stacks ( $1.6 \pm 0.2$ ,  $1.7 \pm 0.2$ , and  $1.6 \pm 0.4 \times 10^{22}$  Am $^2$  for the PISO-1500, SINT-2000 and PADM2M stacks, respectively), and absolute paleointensities measured from transitional lava flows: La Palma ( $1.4 \pm 0.5 \times 10^{22}$  Am $^2$ , Valet et al., 1999) ( $1.9 \pm 0.6 \times 10^{22}$  Am $^2$ , Brown et al., 2009); Tahiti–Punaruu ( $1.6 \pm 0.5 \times 10^{22}$  Am $^2$ , Mochizuki et al., 2011). The 5 ka time interval between 776 and 771 ka characterized in our record by dipole moment minima (highlighted by a dark grey bar at Figs. 8 and 9), therefore provides the best estimate of the MBT duration. Similar VADM ranges for the MBT from different volcanic measurements and from different calibration methods/production simulations further support our evaluation using the independent  $^{10}\text{Be}$  approach. Furthermore, calibrations of different RPI stacks used different strategies: for SINT-2000, Valet et al. (2005) averaged VADM values over 100 ka time intervals, then calculated the time-averaged VADM over the past 800 ka ( $7.46 \pm 1.16 \times 10^{22}$  Am $^2$ ) and used this value to calibrate the 2 Ma RPI stack. Channell et al. (2009) scaled their RPI stack to the mean VADM value of Valet et al. (2005) for

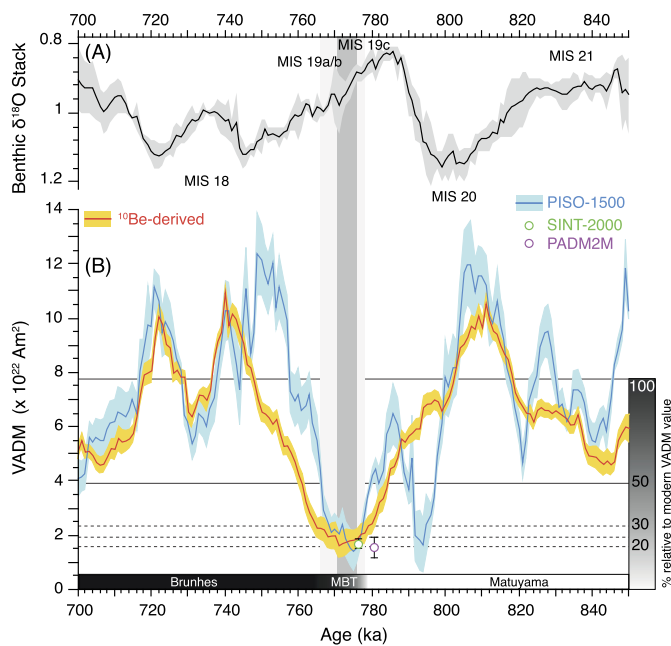


**Fig. 9.**  $^{10}\text{Be}$ -derived GDM reconstruction over the 700–850 ka interval. (A) Stack of the four studied benthic  $\delta^{18}\text{O}$  records. (B) The  $^{10}\text{Be}$ -derived GDM record constructed using the theoretical global  $^{10}\text{Be}$  production rate model of Poluianov et al. (2016) (see Fig. 7) is compared to the calibrated relative paleointensity PISO-1500 stack (Channell et al., 2009) and to average transitional VADM values from the SINT-2000 (Valet et al., 2005) and PADM2M (Ziegler et al., 2011) global RPI stacks. The field percentages are calculated relative to the modern VADM value. A longstanding dipole moment minimum (light grey banding) occurred at 778–766 ka ( $<2.2 \times 10^{22} \text{ Am}^2$ ) and is characterized by a main low interval (average value:  $1.7 \pm 0.4 \times 10^{22} \text{ Am}^2$ ) associated with the MBT within the 771–776 ka (dark grey band) time period.

the last 800 ka and then assigned an intensity of  $7.5 \mu\text{T}$  at IODP Site U1308 (which serves as the reference record for the stack) for the minimum RPI value (at the Cobb Mountain Subchron) arguing that the minimum intensity value corresponds to the likely value of the residual field after total collapse of the axial dipole at times of reversals (Constable and Tauxe, 1996). In the PADM2M stack, a penalized iterative spline model was used for sparse absolute paleointensity data to predict a PADM value at every time point, then estimated the scale needed to transform each RPI series into VADM values (Ziegler et al., 2011). These three calibration procedures agree with our  $^{10}\text{Be}$ -derived calculation to provide a VADM threshold of  $1.7 \pm 0.4 \times 10^{22} \text{ Am}^2$  for the occurrence of the MBT, which corresponds to about 20% of the present dipole moment. Other case studies need to be made before generalizing this evaluation to other polarity reversals or excursions.

## 7. Conclusions

We present new high-resolution authigenic  $^{10}\text{Be}/^9\text{Be}$  ratio (Be-ratio) and benthic  $\delta^{18}\text{O}$  (*Cibicides wuellerstorfi*) records spanning the Matuyama–Brunhes transition. The geographic distribution of the studied sites in the North Atlantic, Indian, and Pacific Oceans allows global scale assessment of related cosmogenic nuclide  $^{10}\text{Be}$  production changes. Astrochronological calibration of  $\delta^{18}\text{O}$  benthic records provides a robust chronological frame over the 700–850 ka time interval. All records include two-fold increases of the Be-ratio through the polarity transition, which supports a common origin linked to the GDM collapse associated with the MBT. These new Be-ratio records together with all other available  $^{10}\text{Be}$ -proxy records obtained from other sediment sequences and the EPICA Dome C Antarctica ice core, confirm the global synchronization of this  $^{10}\text{Be}$  overproduction episode. Our computed age of the MBT

between 776 and 771 ka agrees with the age derived from high-resolution North Atlantic paleomagnetic records (Channell et al., 2010).

We used the atmospheric  $^{10}\text{Be}$  production rate model of Poluianov et al. (2016) to calibrate our Be-ratio stack in terms of global  $^{10}\text{Be}$  production and GDM changes through the last geomagnetic reversal. The two-fold Be-ratio increase corresponds to a global  $^{10}\text{Be}$  atmospheric production increase of more than 300 atoms  $\text{m}^{-2} \text{ s}^{-1}$  triggered by the GDM collapse. This order of magnitude is comparable with that obtained from an atmospheric  $^{10}\text{Be}$  production simulation in modern and zero dipole moment conditions (Heikkilä et al., 2009). The dynamics of our  $^{10}\text{Be}$ -derived GDM reconstruction agree well with the best records obtained from relative (RPI) and absolute (PI) paleointensity measurements. Minimum GDM values between 776 and 771 ka averaging to  $1.7 \pm 0.4 \times 10^{22} \text{ Am}^2$  are similar to the minimum value from models and to VADM values calibrated from RPI stacks or deduced from absolute paleointensities measured on transitional lava flows extruded during the MBT. It is, therefore, a reasonable GDM threshold for the occurrence of geomagnetic reversals. Coupling Be-ratio and oxygen isotope studies on sedimentary sequences provides an accurate means to estimate the age, duration, and dynamics of the last polarity reversal, and enables deciphering of geomagnetic dipole moment for reconstructions of paleomagnetic field variations and geodynamo simulations.

## Acknowledgements

The authors particularly acknowledge Sandrine Choy (CEREGE), Adrien Duvivier (CEREGE) and Anouk Villedieu (LSCE) for samples preparation. We acknowledge Stepan Poluianov (University of Oulu) for his advice on the cosmogenic production model and code. We thank the editor, Martin Frank, Andrew P. Roberts and two anonymous reviewers for very constructive comments that contributed to improve significantly the quality of this paper. The ASTER AMS national facility (CEREGE, Aix en Provence) is supported by INSU/CNRS, ANR through the EQUIPEX “ASTER-CEREGE” action, and IRD. This study is supported by the ERC advanced grant to JPV “GA 339899-EDIFICE” under the ERC’s 7th Framework Program (FP7-IDEA-ERC). The data presented in this study are available within the supporting information and archived at the Pangaea database ([www.pangaea.de](http://www.pangaea.de)).

## Appendix A. Supplementary material

Supplementary material related to this article can be found online at <https://doi.org/10.1016/j.epsl.2018.02.036>.

## References

- Amit, H., Leonhardt, R., Wicht, J., 2010. Polarity reversals from paleomagnetic observations and numerical dynamo simulations. *Space Sci. Rev.* 155, 293–335.
- Bassinot, F.C., Labeyrie, L.D., Vincent, E., Quidelleur, X., Shackleton, N.J., Lancelot, Y., 1994. The astronomical theory of climate and the age of the Brunhes–Matuyama magnetic reversal. *Earth Planet. Sci. Lett.* 126, 91–108.
- Bazin, L., Landais, A., Lemieux-Dudon, B., Toyé Mahamadou Kele, H., Veres, D., Parrenin, F., Martinier, P., Ritz, C., Capron, E., Lipenkov, V., Loutre, M.-F., Raynaud, D., Vinther, B., Svensson, A., Rasmussen, S.O., Severi, M., Blunier, T., Leuenberger, M., Fischer, H., Masson-Delmotte, V., Chappellaz, J., Wolff, E., 2013. An optimized multi-proxy, multi-site Antarctic ice and gas orbital chronology (AICC2012): 120–800 ka. *Clim. Past* 9, 1715–1731.
- Bourlès, D.L., Raisbeck, G.M., Yiou, F., 1989.  $^{10}\text{Be}$  and  $^9\text{Be}$  in marine sediments and their potential for dating. *Geochim. Cosmochim. Acta* 53 (2), 443–452.
- Braucher, R., Guillou, V., Bourlès, D.L., Arnold, M., Aumaitre, G., Keddadouche, K., Nottoli, E., 2015. Preparation of ASTER in-house  $^{10}\text{Be}/^9\text{Be}$  standard solutions. *Nucl. Instrum. Methods Phys. Res., Sect. B, Beam Interact. Mater. Atoms* 361, 335–340.
- Brown, M.C., Gratton, M.N., Shaw, J., Holme, R., Soler, V., 2009. Microwave palaeointensity results from the Matuyama–Brunhes geomagnetic field reversal. *Phys. Earth Planet. Inter.* 173, 75–102.

- Buffett, B.A., Ziegler, L., Constable, C.G., 2013. A stochastic model for palaeomagnetic field variations. *Geophys. J. Int.* 195, 86–97.
- Carcaillet, J.T., Bourlès, D.L., Thouveny, N., 2004. Geomagnetic dipole moment and  $^{10}\text{Be}$  production rate intercalibration from authigenic  $^{10}\text{Be}/^9\text{Be}$  for the last 1.3 Ma. *Geochim. Geophys. Geosyst.* 5 (5), Q05006. <https://doi.org/10.1029/2003GC000641>.
- Carcaillet, J.T., Thouveny, N., Bourlès, D.L., 2003. Geomagnetic moment instability between 0.6 and 1.3 Ma from cosmogenic evidence. *Geophys. Res. Lett.* 30 (15), 1792. <https://doi.org/10.1029/2003GL017550>.
- Channell, J.E.T., 2017. Complexity in Matuyama–Brunhes polarity transitions from North Atlantic IODP/ODP deep-sea sites. *Earth Planet. Sci. Lett.* 467, 43–56.
- Channell, J.E.T., Hodell, D.A., 2017. Comment on Mark et al. (2017): High-precision  $^{40}\text{Ar}/^{39}\text{Ar}$  dating of Pleistocene tuffs and temporal anchoring of the Matuyama–Brunhes boundary. *Quat. Geochronol.* 42, 56–59.
- Channell, J.E.T., Hodell, D.A., Singer, B.S., Xuan, C., 2010. Reconciling astrochronological and  $^{40}\text{Ar}/^{39}\text{Ar}$  ages for the Matuyama–Brunhes boundary in the late Matuyama Chron. *Geochim. Geophys. Geosyst.* 11, Q0AA12. <https://doi.org/10.1029/2010GC003203>.
- Channell, J.E.T., Xuan, C., Hodell, D.A., 2009. Stacking paleointensity and oxygen isotope data for the last 1.5 Myr (PISO-1500). *Earth Planet. Sci. Lett.* 283 (1–4), 14–23. <https://doi.org/10.1016/j.epsl.2009.03.012>.
- Chmeleff, J., von Blanckenburg, F., Kossert, K., Jakob, D., 2010. Determination of the  $^{10}\text{Be}$  half-life by multicollector ICP-MS and liquid scintillation counting. *Nucl. Instrum. Methods Phys. Res. B* 268 (2), 192–199. <https://doi.org/10.1016/j.nimb.2009.09.012>.
- Coe, R.S., Liddicoat, J.C., 1994. Overprinting of natural magnetic remanence in lake sediments by a subsequent high-intensity field. *Nature* 367, 57–59. <https://doi.org/10.1038/367057a0>.
- Coe, R.S., Singer, B.S., Pringle, M.S., Zhao, X., 2004. Matuyama–Brunhes reversal and Kamikatsura event on Maui: paleomagnetic directions,  $^{40}\text{Ar}/^{39}\text{Ar}$  ages and implications. *Earth Planet. Sci. Lett.* 222, 667–684.
- Constable, C., Tauxe, L., 1996. Towards absolute calibration of sedimentary paleointensity records. *Earth Planet. Sci. Lett.* 143, 269–274.
- Frank, M., Schwarz, B., Baumann, S., Kubik, P.W., Suter, M., Mangini, A., 1997. A 200 kyr record of cosmogenic radionuclide production rate and geomagnetic field intensity from  $^{10}\text{Be}$  in globally stacked deep-sea sediments. *Earth Planet. Sci. Lett.* 149 (1–4), 121–129.
- Giacco, B., Regattieri, E., Zanchetta, G., Nomade, S., Renne, P.R., Sprain, C.J., Drysdale, R.N., Tzedakis, P.C., Messina, P., Scardia, G., Sposato, A., Bassinot, F., 2015. Duration and dynamics of the best orbital analogue to the present interglacial. *Geology* 43 (7), 603–606.
- Glatzmaier, G.A., Coe, R.S., 2015. Magnetic polarity reversals in the core. In: *Treatise on Geophysics*, vol. 8, Geomagnetism, second edition. Elsevier, Amsterdam, pp. 279–295. Chapter 11.
- Glatzmaier, G.A., Roberts, P.H., 1995. A three-dimensional self-consistent computer simulation of a geomagnetic field reversal. *Nature* 377, 203–209.
- Hartl, P., Tauxe, L., 1996. A precursor to the Matuyama/Brunhes transition field instability as recorded in pelagic sediments. *Earth Planet. Sci. Lett.* 138, 121–135.
- Heikkilä, U., Beer, J., Feichter, J., 2009. Meridional transport and deposition of atmospheric  $^{10}\text{Be}$ . *Atmos. Chem. Phys.* 9, 515–527.
- Heikkilä, U., von Blanckenburg, F., 2015. The global distribution of Holocene meteoric  $^{10}\text{Be}$  fluxes from atmospheric models. Distribution maps for terrestrial Earth surface applications. GFZ Data Services. <https://doi.org/10.5880/GFZ.3.4.2015.001>.
- Horiuchi, K., Kamata, K., Maejima, S., Sasaki, S., Sasaki, N., Yamazaki, T., Fujita, S., Motoyama, H., Matsuzaki, H., 2016. Multiple  $^{10}\text{Be}$  records revealing the history of cosmic-ray variations across the Iceland Basin excursion. *Earth Planet. Sci. Lett.* 440, 105–114.
- Jicha, B.R., Singer, B.S., Sobol, P., 2016. Re-evaluation of the ages of  $^{40}\text{Ar}/^{39}\text{Ar}$  sanidine standards and supereruptions in the western U.S. using a Noblesse multicollector mass spectrometer. *Chem. Geol.* 431, 54–66.
- Kleiven, H.F., Hall, I.R., McCave, I.N., Knorr, G., Jansen, E., 2011. Coupled deep-water flow and climate variability in the middle Pleistocene North Atlantic. *Geology* 39 (4), 343–346. <https://doi.org/10.1130/G31651.1>.
- Korschinek, G., Bergmaier, A., Faestermann, T., Gerstmann, U.C., Knie, K., Rugel, G., Wallner, A., Dillmann, I., Dollinger, G., von Gostomski Ch, Lieser, Kossert, K., Maiti, M., Poutivtsev, M., Remmert, A., 2010. A new value for the half-life of  $^{10}\text{Be}$  by Heavy-Ion Elastic Recoil Detection and liquid scintillation counting. *Nucl. Instrum. Methods Phys. Res. B* 268 (2), 187–191. <https://doi.org/10.1016/j.nimb.2009.09.020>.
- Kovaltsov, G.A., Usoskin, I.G., 2010. A new 3D numerical model of cosmogenic nuclide  $^{10}\text{Be}$  production in the atmosphere. *Earth Planet. Sci. Lett.* 291 (1–4), 182–188. <https://doi.org/10.1016/j.epsl.2010.01.011>.
- Lal, D., Peters, B., 1967. Cosmic ray produced radioactivity on the Earth. In: *Handbuch der Physik*, vol. XLVI/2. Springer, New York, pp. 551–612.
- Laskar, J., Robutel, P., Joutel, F., Gastineau, M., Correia, A.C.M., Levrard, B., 2004. A long-term numerical solution for the insolation quantities of the Earth. *Astron. Astrophys.* 428 (1), 261–285. <https://doi.org/10.1051/0004-6361:20041335>.
- Lee, M.Y., Chen, C.H., Wei, K.Y., Iizuka, Y., Carey, S., 2004. First Toba supereruption revival. *Geology* 32 (1), 61–64.
- Lee, M.Y., Wei, K.Y., 2000. Australasian microtektites in the South China Sea and the West Philippine Sea: implications for age, size and location of the impact crater. *Meteorit. Planet. Sci.* 35, 1151–1156.
- Leonhardt, R., Fabian, K., 2007. Paleomagnetic reconstruction of the global geomagnetic field evolution during the Matuyama/Brunhes transition: iterative Bayesian inversion and independent verification. *Earth Planet. Sci. Lett.* 253 (1–2), 172–195.
- Lisiecki, L.E., Raymo, M.E., 2005. A Pliocene–Pleistocene stack of 57 globally distributed benthic  $\delta^{18}\text{O}$  record. *Paleoceanography* 20, PA1003. <https://doi.org/10.1029/2004PA001071>.
- Lisiecki, L.E., Raymo, M.E., 2009. Diachronous benthic  $\delta^{18}\text{O}$  responses during late Pleistocene terminations. *Paleoceanography* 24, PA3210. <https://doi.org/10.1029/2009PA001732>.
- Mark, D.F., Renne, P.R., Dymock, R., Smith, V.C., Simon, J.I., Morgan, L.E., Staff, R.A., Ellis, B.S., 2017. High-precision  $^{40}\text{Ar}/^{39}\text{Ar}$  dating of Pleistocene tuffs and temporal anchoring of the Matuyama–Brunhes boundary. *Quat. Geochronol.* 39, 1–23.
- Ménabréaz, L., Thouveny, N., Bourlès, D.L., Deschamps, P., Hamelin, B., Demory, F., 2011. The Laschamp geomagnetic dipole low expressed as a cosmogenic  $^{10}\text{Be}$  atmospheric overproduction at ~41 ka. *Earth Planet. Sci. Lett.* 312 (3–4), 305–317. <https://doi.org/10.1016/j.epsl.2011.10.037>.
- Ménabréaz, L., Bourlès, D.L., Thouveny, N., 2012. Amplitude and timing of the Laschamp geomagnetic dipole low from the global atmospheric  $^{10}\text{Be}$  overproduction: contribution of authigenic  $^{10}\text{Be}/^9\text{Be}$  ratios in west equatorial Pacific sediments. *J. Geophys. Res.* 117 (B11101). <https://doi.org/10.1029/2012JB009256>.
- Ménabréaz, L., Thouveny, N., Bourlès, D.L., Vidal, L., 2014. The geomagnetic dipole moment variation between 250 and 800 ka BP reconstructed from the authigenic  $^{10}\text{Be}/^9\text{Be}$  signature in West Equatorial Pacific sediments. *Earth Planet. Sci. Lett.* 385, 190–205. <https://doi.org/10.1016/j.epsl.2013.10.037>.
- Mochizuki, N., Oda, H., Ishizuka, O., Yamazaki, T., Tsunakawa, H., 2011. Paleointensity variation across the Matuyama–Brunhes polarity transition: observations from lavas at Punaruu Valley, Tahiti. *J. Geophys. Res.* 116, B06103. <https://doi.org/10.1029/2010JB008093>.
- Monaghan, M.C., Krishnaswami, S., Turekian, K.K., 1986. The global-average production rate of  $^{10}\text{Be}$ . *Earth Planet. Sci. Lett.* 76, 279–287.
- Niespolo, E.M., Rutte, D., Deino, A.L., Renne, P.R., 2017. Intercalibration and age of the Alder Creek sanidine  $^{40}\text{Ar}/^{39}\text{Ar}$  standard. *Quat. Geochronol.* 39, 205–2013.
- Nishiizumi, K., Imamura, M., Caffee, M.W., Southon, J.R., Finkel, R.C., McAninch, J., 2007. Absolute calibration of  $^{10}\text{Be}$  AMS standards. *Nucl. Instrum. Methods Phys. Res., Sect. B* 258, 403–413.
- Nomade, S., Bassinot, F., Marino, M., Simon, Q., Dewilde, F., Maiorano, P., Isguder, G., Blamart, D., Girone, A., Scao, V., Pereira, A., Toti, F., Bertini, A., Combourieu-Nebout, N., Peral, M., Bourlès, D.L., Petrosino, P., Ciaranfi, N., in revision. High-resolution foraminifer stable isotope record of MIS 19 at Montalbano Jonico, southern Italy: a window into Mediterranean climatic variability during a low-eccentricity interglacial. *Quat. Sci. Rev.*
- Okada, M., Sugauma, Y., Haneda, Y., Kazaoka, O., 2017. Paleomagnetic direction and paleointensity variations during the Matuyama–Brunhes polarity transition from a marine succession in the Chiba composite section of the Boso Peninsula, central Japan. *Earth Planets Space* 69, 45. <https://doi.org/10.1186/s40623-017-0627-1>.
- Polunianov, S.V., Kovaltsov, G.A., Mishev, A.L., Usoskin, I.G., 2016. Production of cosmogenic isotopes  $^7\text{Be}$ ,  $^{10}\text{Be}$ ,  $^{14}\text{C}$ ,  $^{22}\text{Na}$ , and  $^{36}\text{Cl}$  in the atmosphere: altitudinal profiles of yield functions. *J. Geophys. Res., Atmos.* 121, 8125–8136. <https://doi.org/10.1002/2016JD025034>.
- Railsback, L.B., Gibbard, P.L., Head, M.J., Voarintsoa, N.R.G., Toucanne, S., 2015. An optimized scheme of lettered marine isotope substages for the last 1.0 million years, and the climatostratigraphic nature of isotope stages and substages. *Quat. Sci. Rev.* 111, 94–106.
- Raisbeck, G.M., Yiou, F., Bourlès, D., Kent, D.V., 1985. Evidence for an increase in cosmogenic  $^{10}\text{Be}$  during a geomagnetic reversal. *Nature* 315, 315–317. <https://doi.org/10.1038/315315a0>.
- Raisbeck, G.M., Yiou, F., Cattani, O., Jouzel, J., 2006.  $^{10}\text{Be}$  evidence for the Matuyama–Brunhes geomagnetic reversal in the EPICA Dome C ice core. *Nature* 444 (7115), 82–84. <https://doi.org/10.1038/nature05266>.
- Roberts, A., 2015. Magnetic mineral diagenesis. *Earth-Sci. Rev.* 151, 1–47.
- Roberts, A.P., Winklhofer, M., 2004. Why are geomagnetic excursions not always recorded in sediments? Constraints from post-depositional remanent magnetization lock-in modelling. *Earth Planet. Sci. Lett.* 227, 345–359.
- Roberts, A.P., Tauxe, L., Heslop, D., 2013. Magnetic paleointensity stratigraphy and high-resolution Quaternary geochronology: successes and future challenges. *Quat. Sci. Rev.* 61, 1–16.
- Sagnotti, L., Giaccio, B., Liddicoat, J.C., Nomade, S., Renne, P.R., Scardia, G., Sprain, C.J., 2016. How fast was the Matuyama–Brunhes geomagnetic reversal? A new subcentennial record from the Sulmona Basin, central Italy. *Geophys. J. Int.* 204, 798–812. <https://doi.org/10.1093/gji/ggv486>.
- Schmidt, G., Zhou, L., Wasson, J.T., 1993. Iridium anomaly associated with the Australasian tektite-producing impact: masses of the impactor and of the Australasian tektites. *Geochim. Cosmochim. Acta* 57, 4851–4859.

- Schneider, D.A., Kent, D.V., Mello, G., 1992. A detailed chronology of the Australasian impact event, the Brunhes–Matuyama geomagnetic reversal and global climate change. *Earth Planet. Sci. Lett.* 111, 395–405.
- Simon, Q., Thouveny, N., Bourlès, D.L., Valet, J.P., Bassinot, F., Ménabréaz, L., Guillou, V., Choy, S., Beaufort, L., 2016a. Authigenic  $^{10}\text{Be}/^{9}\text{Be}$  ratio signatures of the cosmogenic nuclide production linked to geomagnetic dipole moment variation since the Brunhes/Matuyama boundary. *J. Geophys. Res., Solid Earth* 121. <https://doi.org/10.1002/2016JB013335>.
- Simon, Q., Thouveny, N., Bourlès, D.L., Nuttin, L., Hillaire-Marcel, C., St-Onge, G., 2016b. Authigenic  $^{10}\text{Be}/^{9}\text{Be}$  ratios and  $^{10}\text{Be}$ -fluxes ( $^{230}\text{Th}_{\text{xs}}$ -normalized) in central Baffin Bay sediments during the last glacial cycle: paleoenvironmental implications. *Quat. Sci. Rev.* 140, 142–162. <https://doi.org/10.1016/j.quascirev.2016.03.027>.
- Simon, Q., Bourlès, D.L., Bassinot, F., Nomade, S., Marino, M., Ciaranfi, N., Girone, A., Maiorano, P., Thouveny, N., Choy, S., Dewilde, F., Scao, V., Isguder, G., Blamart, D., ASTER Team, 2017. Authigenic  $^{10}\text{Be}/^{9}\text{Be}$  ratio signature of the Matuyama–Brunhes boundary in the Montalbano Jonico marine succession. *Earth Planet. Sci. Lett.* 460, 255–267. <https://doi.org/10.1016/j.epsl.2016.11.052>.
- Simon, Q., Bourlès, D.L., Thouveny, N., Horng, C.-H., Valet, J.P., Bassinot, F., Choy, S., 2018. Cosmogenic signature of geomagnetic reversals and excursions from the Reunion event to the Matuyama–Brunhes transition (0.7–2.14 Ma interval). *Earth Planet. Sci. Lett.* 482, 510–524. <https://doi.org/10.1016/j.epsl.2017.11.021>.
- Singer, B.S., Hoffman, K.A., Coe, R.S., Brown, L.L., Jicha, B.R., Pringle, M.S., Chauvin, A., 2005. Structural and temporal requirements for geomagnetic field reversal deduced from lava flows. *Nature* 434, 633–636.
- Singer, B.S., Jicha, B.R., Mochizuki, N., Coe, R.S., 2017.  $^{40}\text{Ar}/^{39}\text{Ar}$  multi-collector revolution and age of the Matuyama–Brunhes boundary. In: GSA Annual Meeting in Seattle. Washington, USA. Paper No. 352-4.
- Smit, J., van Eijden, A., Troelstra, S.R., 1991. Analysis of the Australasian microtektite event, the Toba lake event, and the Cretaceous/Paleogene boundary, Eastern Indian Ocean. *Proc. Ocean Drill. Program Sci. Results* 121, 489–503.
- Suganuma, Y., Okuno, J., Heslop, D., Roberts, A.P., Yamazaki, T., Yokoyama, Y., 2011. Post-depositional remanent magnetization lock-in for marine sediments deduced from  $^{10}\text{Be}$  and paleomagnetic records through the Matuyama–Brunhes boundary. *Earth Planet. Sci. Lett.* 311, 39–52.
- Suganuma, Y., Yokoyama, Y., Yamazaki, T., Kawamura, K., Horng, C.-S., Matsuzaki, H., 2010.  $^{10}\text{Be}$  evidence for delayed acquisition of remanent magnetization in marine sediments: implication for a new age for the Matuyama–Brunhes boundary. *Earth Planet. Sci. Lett.* 296, 443–450. <https://doi.org/10.1016/j.epsl.2010.05.031>.
- Tauxe, L., Herbert, T., Shackleton, N.J., Kok, Y.S., 1996. Astronomical calibration of the Matuyama–Brunhes boundary: consequences for magnetic remanence acquisition in marine carbonates and the Asian loess sequences. *Earth Planet. Sci. Lett.* 140, 133–146.
- Thouveny, N., Carcaillet, J., Moreno, E., Leduc, G., Nérini, D., 2004. Geomagnetic moment variation and paleomagnetic excursions since 400 kyr BP: a stacked record from sedimentary sequences of the Portuguese margin. *Earth Planet. Sci. Lett.* 219, 377–396.
- Tzedakis, P.C., Channell, J.E.T., Hodell, D.A., Kleiven, H.F., Skinner, L.C., 2012. Determining the natural length of the current interglacial. *Nat. Geosci.* 5, 138–141. <https://doi.org/10.1038/ngo1358>.
- Valet, J.P., Bassinot, F., Bouilloux, A., Bourlès, D.L., Nomade, S., Guillou, V., Lopes, F., Thouveny, N., Dewilde, F., 2014. Geomagnetic, cosmogenic and climatic changes across the last geomagnetic reversal from Equatorial Indian Ocean sediments. *Earth Planet. Sci. Lett.* 397, 67–79. <https://doi.org/10.1016/j.epsl.2014.03.053>.
- Valet, J.P., Bassinot, F., Simon, Q., Savranskaia, T., Thouveny, N., Bourlès, D.L., Villedieu, A., submitted. Constraining the age of the last geomagnetic reversal from geochemical and magnetic analyses of Atlantic, Indian and Pacific Ocean sediments. *Earth Planet. Sci. Lett.*
- Valet, J.P., Brassart, J., Quidelleur, X., Soler, V., Gillot, P.Y., Hongre, L., 1999. Paleointensity variations across the last geomagnetic reversal at La Palma, Canary Islands, Spain. *J. Geophys. Res.* 104 (B4), 7577–7598.
- Valet, J.P., Fournier, A., 2016. Deciphering records of geomagnetic reversals. *Rev. Geophys.* 54. <https://doi.org/10.1002/2015RG000506>.
- Valet, J.P., Fournier, A., Courtillot, V., Herrero-Bervera, E., 2012. Dynamical similarity of geomagnetic field reversals. *Nature* 490, 89–94. <https://doi.org/10.1038/nature11491>.
- Valet, J.P., Meynadier, L., Guyodo, Y., 2005. Geomagnetic field strength and reversal rate over the past 2 million years. *Nature* 435, 802–805.
- Valet, J.P., Meynadier, L., Simon, Q., Thouveny, N., 2016. When and why sediments fail to record the geomagnetic field during polarity reversals? *Earth Planet. Sci. Lett.* 453, 96–107. <https://doi.org/10.1016/j.epsl.2016.07.055>.
- Vella, J., Carlut, J., Valet, J.P., Le Goff, M., Soler, V., Lopes, F., 2017. Remagnetization of lava flows spanning the last geomagnetic reversal. *Geophys. J. Int.* 210, 1281–1293.
- von Blanckenburg, F., O’Nions, R.K., Bleshaw, N.S., Gibb, A., Hein, J.R., 1996. Global distribution of beryllium isotopes in deep ocean water as derived from Fe–Mn crusts. *Earth Planet. Sci. Lett.* 141, 213–226.
- von Blanckenburg, F., Bouchez, J., 2014. River fluxes to the sea from the ocean’s  $^{10}\text{Be}/^{9}\text{Be}$  ratio. *Earth Planet. Sci. Lett.* 387, 34–43.
- Wicht, J., Meduri, D.G., 2016. A Gaussian model for simulated geomagnetic field reversals. *Phys. Earth Planet. Inter.* 259, 45–60.
- Wittmann, H., von Blanckenburg, F., Mohtadi, M., Christl, M., Bernhardt, A., 2017. The competition between coastal trace metal fluxes and oceanic mixing from the  $^{10}\text{Be}/^{9}\text{Be}$  ratio: implications for sedimentary records. *Geophys. Res. Lett.* 44. <https://doi.org/10.1002/2017GL074259>.
- Xuan, C., Channell, J.E.T., Hodell, D.A., 2016. Quaternary magnetic and oxygen isotope stratigraphy in diatom-rich sediments of the southern Gardar Drift (IODP Site U1304, North Atlantic). *Quat. Sci. Rev.* 142, 74–89.
- Yamazaki, T., Oda, H., 2005. A geomagnetic paleointensity stack between 0.8 and 3.0 Ma from equatorial Pacific sediment cores. *Geochem. Geophys. Geosyst.* 6, Q11H20. <https://doi.org/10.1029/2005GC001001>.
- Zhou, W., Beck, W., Kong, X., An, Z., Qiang, X., Wu, Z., Xian, F., Ao, H., 2014. Timing of the Brunhes–Matuyama magnetic polarity reversal in Chinese loess using  $^{10}\text{Be}$ . *Geology* 42 (6), 467–470. <https://doi.org/10.1130/G35443.1>.
- Ziegler, L.B., Constable, C.G., Johnson, C.L., Tauxe, L., 2011. PADM2M: a penalized maximum likelihood model of the 0–2 Ma palaeomagnetic axial dipole moment. *Geophys. J. Int.* 184, 1069–1089. <https://doi.org/10.1111/j.1365-246X.2010.04905.x>.